Photon Counting Detector-based Multi-energy Cone Beam CT Platform for Preclinical Small Animal Radiation Research

Xiaoyu Hu[a], Yuncheng Zhong[a], Kai Yang[b], and Xun Jia[a]

[a]innovative Technology Of Radiotherapy Computations and Hardware (iTORCH) Laboratory, Department of Radiation Oncology, University of Texas Southwestern Medical Center, Dallas, TX 75390, USA.

[b]Division of Diagnostic Imaging Physics, Department of Radiology, Massachusetts General Hospital, Boston, MA 02114, USA.

ABSTRACT

We reported our developments of a photon counting detector (PCD) based multi-energy cone beam CT (ME-CBCT) for preclinical small animal radiation research. The development was based on an existing preclinical small animal irradiator that includes a gantry mounted x-ray tube for imaging and radiation experiments in a self-shielded cabinet. We installed a PCD on the gantry and developed the data acquisition, processing, and image reconstruction pipeline to reconstruct CBCT images at three energy channels. We determined the optimal energy thresholds as 26, 56, and 90 keV to achieve uniform signal-to-noise ratio among energy channels. Pixel-based detector response calibration was performed to remove ring artifacts in the reconstructed CBCT images. The average difference between measured x-ray attenuation coefficients of targeted materials from ME-CBCT images and analytically calculated values was 10%. We decomposed the ME-CBCT images into images of water and bone material via an optimization model. The PCD-based ME-CBCT is expected to facilitate critical tasks in preclinical small animal irradiation researches, such as improved accuracy of radiation dose calculations in experiment planning.

Keywords: Photon counting detectors, Cone Beam CT, Small animal irradiation platform

1. INTRODUCTION

Dedicated image-guided small animal irradiation platform plays an essential role in advancing cancer radiation therapy and research.[1] In the current preclinical irradiation platforms, cone beam CT (CBCT) is widely used as an image guidance device to precisely guide the delivery of a radiation beam to the targeted area with sub-millimeter geometric accuracy.[2] Over decades, along with the advancements of preclinical radiobiology researches, there has been a strong growth of the desire for advanced and quantitative CBCT imaging to support tasks such as Monte Carlo-based radiation dose calculation in experimental planning,[1] or identification of certain x-ray imaging contrast agents.[3] To meet these needs, we have previously developed multi-energy CBCT (ME-CBCT) imaging function on a SmART preclinical radiation platform (Precision X-ray Inc., North Branford, CT, USA) via a multiple-scan approach due to the restriction of using the existing flat-panel based CBCT imaging system.[4] However, the inevitably prolonged scan time leads to issues such as animal motion between scans that affects some imaging tasks such as reduced material decomposition accuracy, increased anesthesia use and hence the risks to the animal subject, as well as the increased x-ray radiation dose. One possible solution to overcome this limitation is photon-counting detector (PCD) based multi-energy CBCT. PCD has been asserted having a great potential in delivering more advanced CBCT functions than the widely-employed energy-integrating detectors (EIDs). Compared with EIDs, PCDs do not need to convert the photon into visible light but directly convert the x-ray photon energy to electrical charges in the form of electron-hole pairs.[5] The detected signal is then compared with a calibrated photon energy (threshold), and a count is added when the charge is greater than the specified threshold. This feature enabled by an application-specific integrated circuit (ASIC) allows

Send correspondence to Xun Jia. E-mail: xunjia@jhu.edu

7th International Conference on Image Formation in X-Ray Computed Tomography, edited by Joseph Webster Stayman, Proc. of SPIE Vol. 12304, 123042R
 · 0277-786X · doi: 10.1117/12.2647036

the PCD-based CT system to simultaneously count photons above several selected energy thresholds, hence ME-CBCT in a single scan.

Over the years, significant efforts have been made in evaluating the performance of PCD-based imaging platforms[6] including preclincial imaging systems.[7] However, to our knowledge, PCD-based CBCT dedicated for preclinical radiation research has not been available, although several table-top systems have been previously built.[8] In this paper, we will report our recent developments of a PCD-based ME-CBCT on our preclinical small animal irradiator including the installation of the PCD on the gantry, the optimization of energy thresholds, and the development of a pipeline for data acquisition, processing, image reconstruction, and material decomposition.

2. METHODS

2.1 ME-CBCT setup

The experiment in this work was based on the SmART preclinical radiation platform shown in Fig. 1, which included a rotating C-arm gantry and an small animal couch assembled in a self-shielded cabinet. The gantry can perform CBCT scanning using an x-ray tube (Comet iVario 225 kV, JME Ltd, Suffolk, UK) mounted on the gantry and an amorphous silicon flat-panel detector (FPD) (XRD 0820 AN3-ES, Perkin-Elmer, Wiesbaden, Germany). An XC-Thor Cadmium telluride (CdTe) PCD (Direct Conversion AB, Sweden) was mounted on an aluminum frame attached to the gantry. The PCD has an active sensor area of 51.2×100.0 mm^2 with a 0.1×0.1 mm^2 pixel size. The source to isocenter distance was 30.5 cm and source to detector distance was 44.2 cm. This PCD was able to output the number of photon counts for each pixel above a user-specified energy threshold T for a time interval Δt.

We used a 100 kVp x-ray beam for CBCT data acquisition, with a rotation time of 1 min. The data acquisition of the PCD was controlled via the Application Programming Interface provided by the vendor. Specifically, we triggered the PCD to acquire projection data at a frequency of 30 frame/sec and each data frame receive photons for $\Delta t = 20$ msec. The remaining ~ 13 msec time interval was allocated for data processing and readout. The energy threshold T was set to sequentially cycle through three energy thresholds T^l, $l = 1, \cdots, 3$. PCD operated under anti-coincidence high sensitivity mode for all acquisitions. For each projection, the projection angle was read out from the encoder of the gantry motor. With this setting, we acquired 600 projection images for each energy threshold.

The workflow covered by this study is summarized in Fig. 2. We will present details of key steps in subsequent sections.

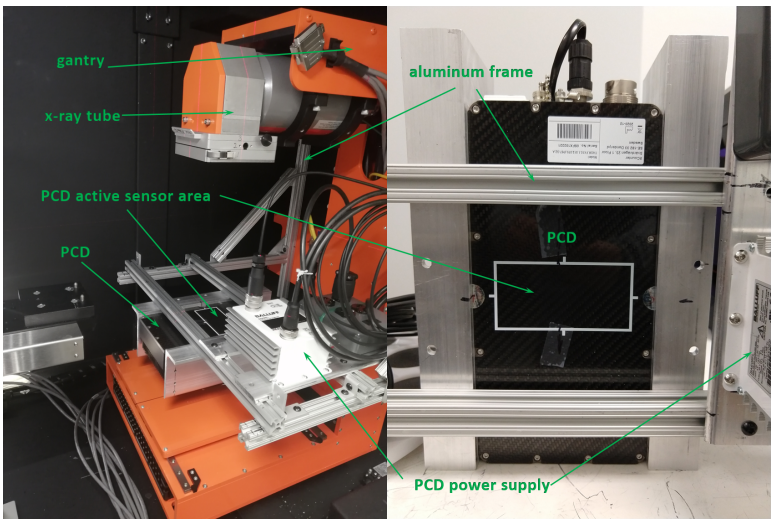

Figure 1. Installation of the PCD on the SmART preclinical radiation platform (left) and the front view of of the PCD (right).

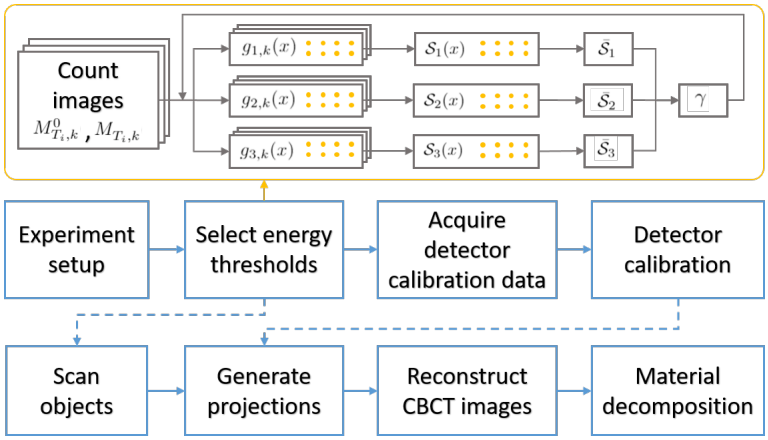

Figure 2. Flowchart of PCD-based ME-CBCT imaging procedures.

2.2 Selection of energy thresholds

The lowest energy threshold T_1 was set to be 26 keV to avoid electronic noises.[9] The other two energy thresholds were determined to balance signal-to-noise ratio (SNR) in log-transformed projection images of all three energy channels, as the SNRs are directly related to those of the subsequently reconstructed images from each channel. As such, we acquired air projection images at 0 degree gantry angle under 3 mA for $N_t = 42$ thresholds T_i, $i = 1, \ldots, N_t$ ranged from 28 to 110 keV, with increment of 2 keV. Note that the thresholds were nominal input values to the PCD, therefore our search range went beyond the 100 kVp used. At every threshold T_i, we acquired $N_f = 200$ projections and denote the count image $M^0_{T_i,k}(x)$, where x is the index of each pixel, $k = 1, 2, ..., N_f$.

For a given threshold combination T^l, $l = 1, 2, 3$ selected among possible T_i, $i = 1, \ldots, N_t$ values, the count images at the three energy channels $E_1 = [T^1, T^2]$ keV, $E_2 = (T^2, T^3]$ keV and $E_3 = (T^3, 100]$ keV, were $C^0_{l,k}(x) = M^0_{T^l,k}(x) - M^0_{T^{l+1},k}(x)$ for $l = 1, 2$ and $C^0_{3,k}(x) = M^0_{T^3,k}(x)$. Note that we wrote the upper bound 100 keV in the third energy channel because of the 100 kVp x-ray beam, yet in practice this channel represents photons counts with energy above the threshold T^3. Following the same procedure, we acquired projection images of a CT calibration phantom, denoted as $C_{l,k}(x)$ for the energy channel l and frame k.

We then computed the log-transformed projection image $g_{l,k}(x) = -\ln[C_{l,k}(x)/\langle C^0_l(x)\rangle]$, where $\langle C^0_l(x)\rangle$ is the averaged counts of the air projection images over all frames. Using the repeatedly acquired 200 projections, we calculated the mean and standard deviation of $g_{l,k}(x)$, denoted as $\bar{g}_l(x)$ and $\sigma_{g_l}(x)$, respectively. Finally, the SNR at coordinate x was calculated as $\mathcal{S}_l(x) = \bar{g}_l(x)/\sigma_{g_l}(x)$. We averaged $\mathcal{S}_l(x)$ over 100 pixels inside the phantom region on the projection image, and denoted the averaged SNR as $\bar{\mathcal{S}}_l$. It was our objective to find proper thresholds such that $\bar{\mathcal{S}}_l$ approximately equal among all energy channels $l = 1, 2, 3$. As such, we considered the metric $\gamma = \max_l \bar{\mathcal{S}}_l / \min_l \bar{\mathcal{S}}_l$. We enumerated all possible combinations of thresholds T^2 and T^3, and found out the combination that minimized γ as the optimal thresholds for subsequent studies.

2.3 Detector calibration

To calibrate the non-uniform pixel responses of PCD, we acquired air scan under the threshold-sweeping mode as in the actual CBCT scan using the energy thresholds determined from Sec. 2.2. We repeated this with x-ray tube current I in the range of [0, 3.4] mA with 0.2 mA increment. Let us denote the count image at energy threshold T^l, $l = 1, \ldots, 3$ with the jth tube current I^0_j, $j = 1, 2, ...$, as $M^0_{l,j}(x)$. Note that we repeatedly acquired 200 frames and took the average of these frames to reduce noise. Count images $C^0_{l,j}(x)$ at the three energy channels were computed by taking the difference between data with subsequent energy thresholds.

With the count images acquired for each energy channel $l = 1, 2, 3$ and tube current level $j = 0, 1, 2, ...$, for each pixel x and energy channel, we fit the tube current as a function of counts using I^0_j and $C^0_{l,j}(x)$ in a polynomial form. The coefficient of determination R^2 was used to evaluate the goodness of the fitting model. In the fitting procedure, we gradually increased the number of polynomial order, until the resulting R^2 reached $R^2_c = 0.9999$. If this was not achievable at 4^{th} order polynomial, the pixel was considered as a 'dead pixel'.

2.4 Image processing, reconstruction and material decomposition

After data acquisition of a CBCT scan, we converted raw count images $C_l(x,\theta)$ of energy channel l to the corresponding images of current $I_l(x,\theta)$ using the established calibration model of each pixel. Here we explicitly write the projection angle θ. In this step, nearest-neighbor interpolation was applied to handle all 'dead pixels'. For each flat-fielded projection image at angle θ, we identified a region that was not blocked by the phantom and computed the averaged pixel value in this region as the air norm $I_l^0(\theta)$. Compared to using the nominal tube current in the scan as the air norm, this approach deriving $I_l^0(\theta)$ considered the tube current fluctuation among projections during the CBCT data acquisition.

After these stpes, we computed the projection image $g_l(x,\theta) = -\ln[I_l(x,\theta)/I_l^0(\theta)]$. Finally, CBCT image $\mathbf{f} = (f_1, f_2, f_3)^\top$ were reconstructed using the projection data and the GPU-based Feldkamp-Davis-Kress (FDK) reconstruction code,[10,11] where f_l, $l = 1, 2, 3$ represents reconstructed image of energy channel l.

In this study, we considered a two-material decomposition model that expressed each image voxel as a linear combination of two basis materials: water and bone. However, with three energy channels, in principle, it is possible to perform three-material decomposition. With our model, $\mathbf{f} = \mathbf{A}\mathbf{m}$, where $\mathbf{m} = (m_w, m_b)^\top$ is a two-component image representing mass density image of the two basis materials, and $\mathbf{A} \in \mathcal{R}^{(3\times 2)}$ is the system matrix. The two columns of $\mathbf{A}$ are x-ray mass attenuation coefficients of corresponding materials in the three energy channels, which was obtained in the reconstructed CT calibration phantom images. To solve for the material images without amplifying noise, we performed material decomposition by solving an optimization problem

$$\mathbf{m} = \underset{\mathbf{m}}{\operatorname{argmin}} \frac{1}{2}\|\mathbf{A}\mathbf{m} - \mathbf{f}\|_2^2 + \lambda\|\nabla\mathbf{m}\|_1, \tag{1}$$

where the first term of the objective function ensured fidelity of the solution to the CBCT images, and the second one was a Total variation regularization term to reduce noise while preserving edges in the solution. λ is a weighting factor controlling the relative importance of the two terms. Note that the operator ∇ was applied to the spatial direction only. This model was solved with the Alternating Direction Method of Multipliers.

2.5 Evaluation

Two phantoms (SmART Scientific Solutions B.V., Maastricht, Netherlands) were utilized to calibrate the ME-CBCT system and evaluate the imaging procedure and image quality. The first one was a preclinical CT calibration insert phantom that contained 10 inserts of different materials plugged into a 30 mm diameter background base representing water. After the CBCT images were reconstructed, we picked two regions of interest with water and bone materials and used the average voxel values normalized by the known material density to construct the material decomposition system matrix $\mathbf{A}$. We then decomposed the CBCT images into the two material images using the model in Eq. (1). The second phantom was a plastinated mouse specimen. Due to the small size of the PCDs (5.0 cm along the rotation axis), only the head was scanned.

3. RESULTS

3.1 Energy thresholds and detector calibration

With the method described in Sec. 2.2, we computed the SNR ratios γ for all threshold combinations of (T^2, T^3). The SNR ratio that was closest to 1 was $\gamma = 1.05$, when the two energy thresholds were $T^2 = 56$ keV and $T^3 = 90$ keV. The corresponding SNRs of projection images were 7.07, 7.32 and 6.98 for the three energy channels, respectively.

Fig. 3 presents the impacts of detector calibration. Without calibration, we can clearly see different detector sub-panels to assemble the entire detector. The boundaries among panels would cause ring artifacts in the reconstructed images. We selected two regions of interest (ROIs) that were not blocked by the phantom. Due to flat x-ray beam fluence, the projection data in these two ROIs are expected to be the same. However, without calibration, we observed a large difference between the raw counts in the two ROIs across all projection angles. The calibration step was able to reduce this discrepancy. The fluctuation among projections was ascribed to x-ray tube output fluctuation, which was taken care of before image reconstruction by the choice of projection-specific air norm.

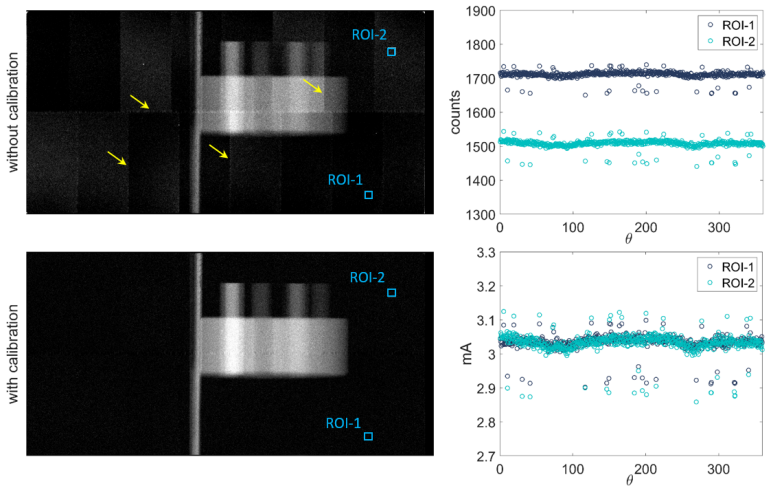

Figure 3. Left: projection images at $\theta = 90$ degree in energy channel E_1 with and without detector calibrations; blue boxes show the location of two ROIs. Right-top: average counts of the two ROIs. Right-bottom: averaged mA of the two ROIs after detector calibration.

3.2 CBCT images and material decomposition

The reconstructed CBCT images of the CT calibration insert phantom and the mouse phantom with three energy channels are shown in Fig. 4. The object contrast reduced with increasing photon energies. For the calibration phantom, we compared measured x-ray attenuation coefficients and those computed by averaging the known x-ray attenuation data weighted by x-ray beam spectrum in the three energy channels. The difference was 10% on average. The difference can be ascribed to multiple factors including the reconstruction model, the discrepancy between nominal and actual energy thresholds, the ignored detector response variation over energy, etc.

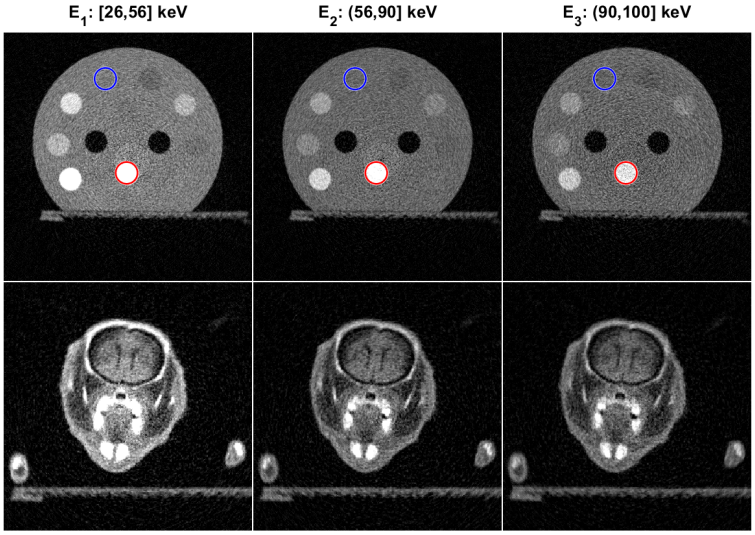

Figure 4. CBCT images of the CT calibration insert phantom (top) and the plastinated mouse specimen (bottom) in the three energy channel. Display window: [0,0.5] cm^{-1}. The blue and red circles indicate the solid water and the bone basis materials.

To perform image-based material decomposition, we selected solid water and bone as two basis materials, and obtained the attenuation coefficients by averaging the voxel values over the corresponding ROIs indicated by the blue and red circles in Fig. 4. The mass attenuation coefficients in the three energy channels were $[0.240, 0.198, 0.186]$ cm^2/g and $[0.489, 0.296, 0.261]$ cm^2/g for water and bone materials, respectively.

Fig. 5 presents the material images of water and bone of CT calibration insert phantom and the plastinated mouse phantom in the axial plane. The two basis materials were differentiated clearly in the material images. Note that the animal skin also appeared in the bone image. The manufacture process of the plastinated mouse caused accumulation of polymer materials at the skin, which appeared as bone-like materials under x-ray imaging.

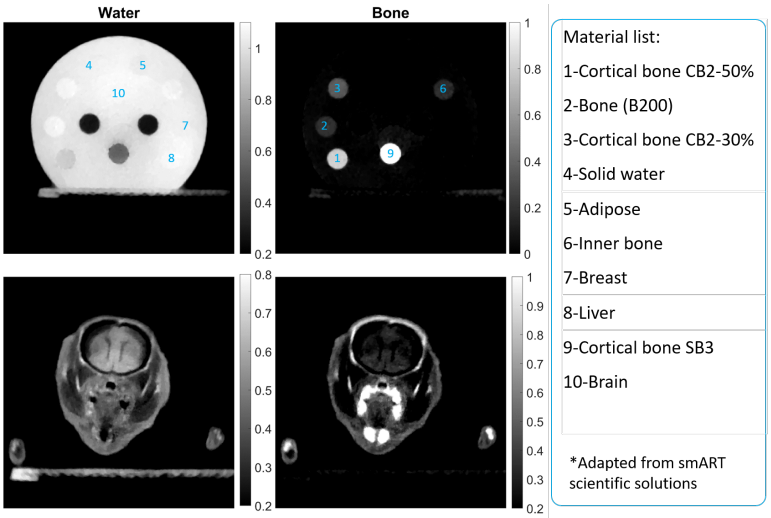

Figure 5. Water (left) and bone (right) maps of the CT calibration insert phantom (top) and the plastinated mouse specimen in the axial plane (bottom).

4. CONCLUSION AND DISCUSSIONS

In this work, we reported our initial study on a PCD-based CBCT for a preclinical small animal irradiation platform. We developed the data acquisition, processing, and image reconstruction pipeline to reconstruct CBCT images at three energy channels. We determined the optimal energy thresholds of 26 keV, 56 keV, and 90 keV to equalize SNR among energy channels. The average difference between measured x-ray attenuation coefficient from ME-CBCT images and calculated values was 10%. We decomposed ME-CBCT images into images of water and bone via an optimization model.

This study only serve as the preliminary step to enable PCD-based ME-CBCT function on a preclinical small animal irradiation platform. Despite the initial results achieved so far, there are a number of task down the road to further characterize and improve this system. For instance, the current CBCT reconstruction assumed an ideal circular trajectory, but the actual trajectory is known to deviate from this ideal case due to gravity. Geometry calibration is hence needed to improve geometry accuracy and resolution of reconstructed CBCT images. Additionally, the detector calibration can be improved via deep learning neural networks.[12,13] The method of selecting energy thresholds proposed in this work was based on the objective of balancing the SNRs over all energy channels. In general, the choice of energy thresholds depends on the specific applications. One of the intended use of this ME-CBCT system is to visualize low-concentration gold nanoparticles, which requires optimization of energy thresholds for that task. Lastly, the utility of the CBCT system in terms of supporting preclinical radiobiology studies will be demonstrated in specific tasks, such as improvement in radiation dose calculations in experiment planning.

REFERENCES

[1] Verhaegen, F., Granton, P., and Tryggestad, E., "Small animal radiotherapy research platforms," *Physics in Medicine & Biology* **56**(12), R55 (2011).

[2] Clarkson, R., Lindsay, P., Ansell, S., Wilson, G., Jelveh, S., Hill, R., and Jaffray, D., "Characterization of image quality and image-guidance performance of a preclinical microirradiator," *Medical physics* **38**(2), 845–856 (2011).

[3] Hainfeld, J. F., Dilmanian, F. A., Slatkin, D. N., and Smilowitz, H. M., "Radiotherapy enhancement with gold nanoparticles," *Journal of pharmacy and pharmacology* **60**(8), 977–985 (2008).

[4] Huang, Y., Hu, X., Zhong, Y., Lai, Y., Shen, C., and Jia, X., "Improving dose calculation accuracy in preclinical radiation experiments using multi-energy element resolved cone-beam ct," *Physics in Medicine & Biology* **66**(24), 245003 (2021).

[5] Fritz, S., *Characterization of photon counting CZT detectors for medical x-ray imaging and spectroscopy*, PhD thesis, Louisiana State University (2011).

[6] Leng, S., Zhou, W., Yu, Z., Halaweish, A., Krauss, B., Schmidt, B., Yu, L., Kappler, S., and McCollough, C., "Spectral performance of a whole-body research photon counting detector CT: quantitative accuracy in derived image sets," *Physics in Medicine & Biology* **62**(17) (2017).

[7] Schlomka, J. P., Roessl, E., Dorscheid, R., Dill, S., Martens, G., Istel, T., Bäumer, C., Herrmann, C., Steadman, R., Zeitler, G., Livne, A., and Proksa, R., "Experimental feasibility of multi-energy photon-counting k-edge imaging in pre-clinical computed tomography," *Physics in Medicine and Biology* **53**, 4031–4047 (jul 2008).

[8] Richtsmeier, D., Dunning, C., Iniewski, K., and Bazalova-Carter, M., "Multi-contrast k-edge imaging on a bench-top photon-counting ct system: acquisition parameter study," *Journal of Instrumentation* **15**(10), P10029–P10029 (2020).

[9] Flohr, T., Ulzheimer, S., Petersilka, M., and Schmidt, B., "Optimization of k-edge imaging with spectral ct," *Chinese Journal of Academic Radiology* **2**, 19–34 (2020).

[10] Feldkamp, L. A., Davis, L. C., and Kress, J. W., "Practical cone-beam algorithm," *Josa a* **1**(6), 612–619 (1984).

[11] Jia, X., Lou, Y., Li, R., Song, W. Y., and Jiang, S. B., "Gpu-based fast cone beam ct reconstruction from undersampled and noisy projection data via total variation," *Medical physics* **37**(4), 1757–1760 (2010).

[12] Li, M., Rundle, D. S., and Wang, G., "X-ray photon-counting data correction through deep learning," (2020).

[13] Shen, C., Nguyen, D., Zhou, Z., Jiang, S. B., Dong, B., and Jia, X., "An introduction to deep learning in medical physics: advantages, potential, and challenges," *Physics in Medicine & Biology* **65**(5), 05TR01 (2020).